ROYAL SOCIETY
OF CHEMISTRY

COMMUNICATION

Check for updates

Selective Li ion transport *via* interpenetrated crystal growth on ZIF-8 seeded nanocomposite membranes†

Benjamin Clayville,[a] Ji Yong Choi, [ID][b] Christian Wagner,[b] William Warren[b] and Jihye Park [ID] *[ab]

ZIF-8 based poly(vinylidene) difluoride (PVDF) nanocomposite mixed matrix membranes (MMMs) were successfully prepared *via* post-synthetic seeded growth of the ZIF-8. PVDF and 5s-MMMs, before ZIF-8 crystallization, exhibit no diffusional selectivity towards Li ions, with intrinsic hydrophobicity and ion conductivity on the order of 10^{-12} S cm^{-1}. On the other hand, crystallized 5c-MMMs with greater hydrophilicity, exhibit diffusional selectivity favoring Li over Na and K ions, with ion conductivities on the order of 10^{-8} S cm^{-1}, owing to the densely interpenetrated morphology of ZIF-8 in and on the membrane, controlling mass transport at selective crystal facets.

Introduction

Lithium (Li) garners increasing significance as an essential element. With expanding reliance on Li-ion battery materials and the pursuit of next generation energy dense battery materials, new methodologies to efficiently harness Li are imperative.[1,2] Leveraging controlled mass transport achieved with ion-selective membranes, aqueous lithium deposits can be targeted with greater energy efficiency.[3,4] Enabling size-sieving effects, observed in nano-porous materials, ion exchange membranes, reverse osmosis membranes, and ion rectifying membranes, have realized promising utility in selective ion transport.[3] However, a faradaic reliance on ion exchange processes can drive energy inefficient separations and lead to chemical degradation, while osmotic processes remain energy intensive, hindering their utility towards efficient Li extraction.[5,6]

Zeolitic imidazolate frameworks (ZIFs) have exhibited remarkable properties in controlling mass transport, realizing highly efficient diffusion-induced molecular separations.[7,8]

Among ZIFs, the ZIF-8, constructed from a sodalite cage with 11.6 Å pores, establishes uniform pore apertures of 3.4 Å, coinciding with the hydrated diameters of alkali cations (Fig. 1A).[9] This geometry facilitates the selective transport of Li ions in aqueous environments *via* the subnanoporous sieving effect.[10] A phenomenon that arises with characteristic network interactions between MOF structures and the unique hydration shells of respective alkali ions (Fig. 1B).[11,12] Unlike MOFs with channelled-pore structures (*e.g.*, UiO-66, MOF-5, *etc.*), ZIF-8 exhibits a caged-pore structure, facilitating dynamic ion dehydration responses with diffusion.[13] Additionally, large

Jihye Park is an Assistant Professor of Chemistry at the University of Colorado Boulder, whose group started in 2020. She received her PhD in Chemistry from Texas A&M University in 2016. Subsequently, she conducted her postdoctoral research in chemical engineering at Stanford University as a Dreyfus Environmental Chemistry Postdoctoral Fellow. Her current research interest revolves around methodology development to functionalize conjugated porous

Jihye Park

framework materials. Her group leverages synthetic tunability to manipulate the material's physical (e.g., length-scale, morphology, dimension) and electronic properties to understand charge transport/ transfer processes. The emergent optical and electrical properties are used as chemical tools to understand their roles in targeted applications, including electrochemical energy storage/conversion and electronic/photonic devices.

[a] Materials Science & Engineering Program, University of Colorado Boulder, Boulder, Colorado 80303, USA. E-mail: jihye.park@colorado.edu

[b] Department of Chemistry, University of Colorado Boulder, Boulder, Colorado 80309, USA

13816 | *J. Mater. Chem. C,* 2024, **12**, 13816–13821

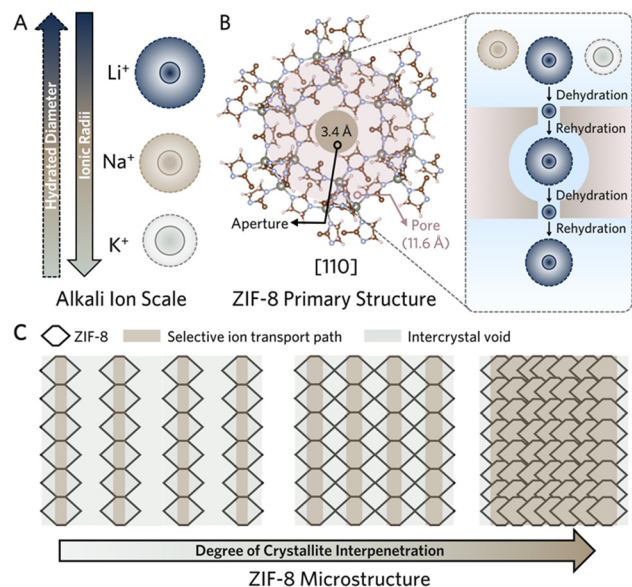This journal is © The Royal Society of Chemistry 2024

Fig. 1 (A) Relative scale of ionic and hydrated alkali metal cations. (B) [110] facet of the ZIF-8 and schematic of ion transport. (C) Strategies to mitigate transport through intercrystal void by targeting continuous morphologies of interpenetrated ZIF-8 crystallites.

pore diameter-aperture ratios allow for the rehydration of partially dehydrated ions, and potentially extend the selective sieving behavior across the structure with increased dehydration events (Fig. 1B, right).

Suppressing alternative, less resistive, transport pathways is imperative to ensure effective control of mass transport through subnanoporous apertures. Intrinsic limitations to processing dry powders, including ZIF-8, drive random crystallite orientations and aggregation of polycrystalline samples, giving rise to nonselective void space at microporous intercrystallite boundaries (Fig. 1C, gray) and leading to low Li ion selectivity.[5] Therefore, it is crucial to consider the continuity of the microstructure. Common approaches to remove intercrystallite void space involve incorporating the MOF crystallites as sieves in polymer matrices, leveraging strong chemisorption and/or physisorption of MOFs to the polymer. However, the resulting composites often substitute microporous intercrystallite void space for larger void space arising from the polymer morphology.[14]

To overcome this issue, continuously interpenetrated ZIF-8 surfaces have been thoroughly investigated to enhance mass transport control across diverse separations.[11,15–19] The morphology reduces the void space between crystallites *via* the intergrowth of terminal crystal facets, thus realizing significantly greater framework density along crystallite–crystallite boundaries (Fig. 1C, right). This approach would suppress transport in mesoscale polymer cavities and polymer-crystallite interfaces as well as the micro-scale intercrystallite voids. As a result, ion transport occurs through the MOF crystal facets facilitating the network aperture-derived selective ion partial dehydration. Several methodologies have enabled intergrown morphologies of the ZIF-8 on supports. However,

inorganic supports still reign dominant while few available polymeric MOF-composites commonly rely on extensive surface functionalization to produce an ultra-thin layer of MOFs.[18–21]

Herein, we present a facile method for fabricating ZIF-8-based mixed matrix membranes (MMMs) to realize Li ion selective diffusion in aqueous conditions. We rationalized poly(vinylidene) difluoride (PVDF) as a suitable substrate for selective ion transport.[22] By compositing PVDF, possessing intrinsic hydrophobicity much greater than typical MOF components, we attempt to thermodynamically drive aqueous transport through MOF-based sieves. Additionally, we expect PVDF's mechanical flexibility and proven compatibility with ZIF-8 to yield a robust MOF-based MMM.[23,24] We chose a nanoscale ZIF-8 as a seed for even dispersion in the PVDF, endowing greater uniformity of the interpenetrated crystal growth.[22] The resulting membrane exhibited transport selectivity favoring Li over two other competing alkali cations; sodium (Na^+) and potassium (K^+) ions in an aqueous solution. Specifically, intergrown ZIF-8 in the MMM facilitates ion transport pathways through the aperture of the ZIF-8 network and increased the relative composite hydrophilicity, leading to substantial enhancements in both Li ion selectivity and conductivity.

Results and discussion

Fabrication and crystallization of MMMs

We synthesized the nanocrystalline ZIF-8 seeds according to an established solvothermal procedure with minimal modification (synthetic details are provided in the ESI†).[25] We characterized the nanocrystalline ZIF-8 with powder X-ray diffractions (PXRD), N_2 sorption isotherms, Fourier transform infrared spectroscopy (FTIR), and scanning electron microscopy (SEM), confirming highly crystalline rhombic dodecahedral ZIF-8 crystallites, of less than 100 nm in size (Fig. S1, ESI†).

The ZIF-8 composite MMM, targeted to be 5 wt% ZIF-8, was then fabricated by compositing the nanocrystalline ZIF-8 with PVDF in *N*,*N*-dimethylformamide (DMF) and acetone (v/v = 1 : 5) at 85 °C, followed by blade coating onto a stencilled glass slide substrate wherein thermally induced phase inversion occurred concurrently with solvent evaporation (Fig. S2A, ESI†).[26,27] The ZIF-8 seeded nanocomposite membrane is denoted as 5s-MMM. To grow interpenetrated ZIF-8 in the membrane, the 5s-MMM was exposed to a sodium formate modulated ZIF-8 crystallization, resulting in the crystallized, 5c-MMM (Fig. S2B, ESI†).[19] The crystallization was allowed for 16 hours, followed by extensive washing with methanol–water solution (Fig. 2A).

We confirmed the composition and structure of the ZIF-8 within the composite by PXRD, proton nuclear magnetic resonance spectroscopy (^1H NMR), and FTIR. As shown in Fig. 2B, ZIF-8's diffraction pattern was evident in both 5s-MMM and 5c-MMM, with the 5c-MMM exhibiting a notable increase in intensity, indicating a higher ZIF-8 content in the composite. These results proved the compatibility between ZIF-8 and PVDF and their stability throughout the composite fabrication process.
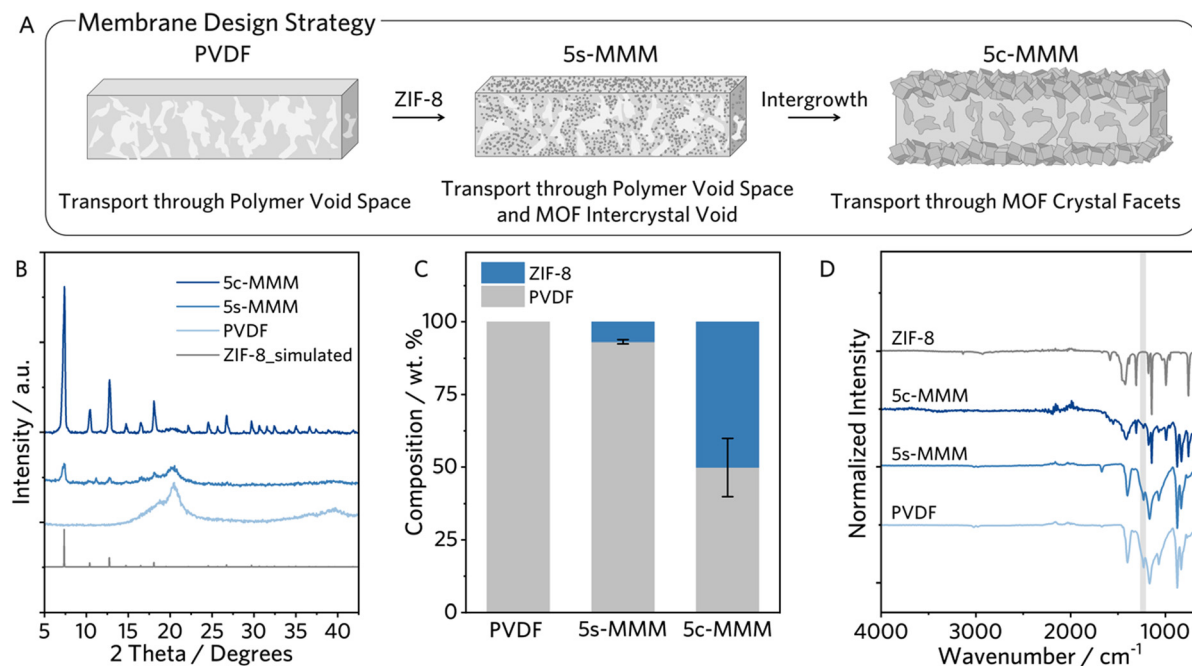
Fig. 2 (A) Membrane design strategy. (B) PXRD, (C) estimated composition, and (D) FTIR of PVDF, 5s-MMM, and 5c-MMM. Composition is determined by ^{1}H NMR digestion experiment.

To support this, we quantitatively probe the relative composition of PVDF and ZIF-8 by ^{1}H NMR digestion analysis. Comparison of the proton integration of PVDF and of 2-methylimidazole from the NMR spectra allowed for a quantitative estimation of the total composition (Fig. S3, S4 and Table S1, ESI†). The 5s-MMM yielded an expected ZIF-8 composition, ∼7 wt%, while the post-synthetic crystallization process drastically altered the membrane composition, increasing the ZIF-8 composition by 6-fold (Fig. 2C). A dominant PVDF vibration at 1232 cm^{-1}, characteristic of the γ-phase, is observed in FTIR of PVDF and the 5s-MMM, reasonable given their low temperature processing (Fig. 2D, highlighted in gray).[28] In addition, the FTIR spectrum of the 5c-MMM largely resembles the characteristic absorptions of the pristine ZIF-8, corroborating the ZIF-8 dominant composition. Interestingly, IR absorptions corresponding to PVDF are largely perturbed by the post-synthetic crystallization, significantly reducing in intensity and width, further supporting the structural rigidity of the 5c-MMM (Fig. 2D).

MMM microstructural evolution

We further characterized the morphology and distribution of ZIF-8 in MMMs *via* SEM. The PVDF membrane exhibited a characteristic dense surface layer with a mesoporous spherulitic morphology (Fig. 3A). Following ZIF-8 seeding, the 5s-MMM showed a similar morphology with much-increased porosity compared to the pristine PVDF (Fig. 3B). This is attributed to the ZIF-8 seeds disturbing both intermolecular PVDF-PVDF chain interactions and PVDF solvation properties during the phase inversion process.[23,29] Leveraging high resolution field emission SEM (FE-SEM), the ZIF-8 particles were observed to coat the surfaces of the PVDF webbing in crystal sizes of ∼100 nm. Interestingly, the post-synthetic crystallization process rigidified the matrix, removing the void space and destroying the mesoporosity persistent in the PVDF and 5s-MMM. The resulting 5c-MMM adopts a dense and continuous morphology in the bulk membrane (Fig. 3C).

Next, we confirmed compositional distribution and the extent of crystallization within the MMM through cross-
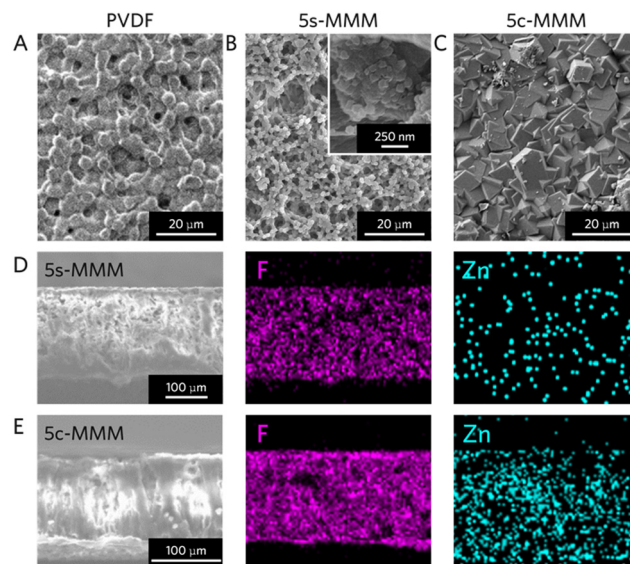

Fig. 3 Surface SEM image of (A) PVDF, (B) 5s-MMM, and (C) 5c-MMM. Inset in (B): FE-SEM detailing nanocrystalline ZIF-8. Cross-sectional SEM image of (D) 5s-MMM and (E) 5c-MMM with high resolution F and Zn mapping, respectively.

13818 | *J. Mater. Chem. C*, 2024, **12**, 13816–13821

This journal is © The Royal Society of Chemistry 2024

sectional energy dispersive X-ray (EDX) mapping. Fluorine (F) mapping was carried out to provide both compositional and topological contrast between ZIF-8 and the surrounding PVDF in the MMMs (Fig. 3D and E). In the 5s-MMM, we observed an even distribution of zinc (Zn) throughout the membrane, implying effective seeding of the PVDF nanocomposite with nanocrystalline ZIF-8 (Fig. 3D). After post-synthetic crystal growth, the Zn density increased homogeneously, indicating successful crystallization occurs deep within the composite matrix, plugging macroscopic void space in the MMM with densely interpenetrated ZIF-8 crystallites (Fig. 3E).

Evaluation of selective ion transport

The interactions between water and the MMMs are crucial due to the aqueous nature of ionic separations. Therefore, the hydrophilicity of the MMMs could drastically affect the current density of respective aqueous ionic concentration currents. To better understand the relative surface hydrophilicity of each MMM, we observed the surface contact angles with deionized (DI) water. We observed that the ZIF-8 seeds in the 5s-MMM minimally perturb the surface properties from the neat PVDF surface, decreasing $2°$ despite a rougher spherulitic surface morphology (Fig. 4A). On the other hand, the 5c-MMM exhibited a dramatic increase in surface hydrophilicity, with a much-reduced contact angle from PVDF and 5s-MMM, over $40°$, suggesting significantly stronger surface interactions with water.

We performed water uptake experiments in the liquid state to corroborate the increased surface hydrophilicity of the 5c-MMM with that of the respective internal surface area (see ESI† for details). We calculated the mass difference between a dry state, achieved with high vacuum drying for 2 hours, and a hydrated state, after submerging the MMMs in deionized water for 48 hours at room temperature.

Given the intrinsic hydrophobicity of PVDF, a negligible mass change of 0.8% $\pm$ 0.4% was found unsurprisingly (Table S2, ESI†). The 5s-MMM yielded a slightly greater water uptake, 6% $\pm$ 1.6%, potentially realized with the increased hydrophilicity and porosity from the webbed composite morphology, as expected from the presence of ZIF-8 (Table S3, ESI†).[29] The 5c-MMM exhibited a notable mass increase of 29% $\pm$ 3.2% after submersion in water (Table S4, ESI†), highlighting the enhancement of the composite hydrophilicity with the crystallization of ZIF-8 on the membrane.

Encouraged by these results, we investigated the ion transport properties of the membranes in an electrochemical H-cell (Fig. 4B and Fig. S5, ESI†). The ion transport was determined by constructing a unary ion concentration gradient of 0.1 M across the MMM sample (Fig. 4B), wherein the gradient induced ion diffusion was allowed to occur for a given period between 1 to 12 hours. We conducted linear sweep voltammetry (LSV) to observe the mass transport limited conductance of the cell, using an Ohmic extrapolation of the time dependent linear current–voltage curve. The ion conductance was then normalized to the geometry and thickness of the MMM sample to extrapolate the respective ion conductivity. We referenced the
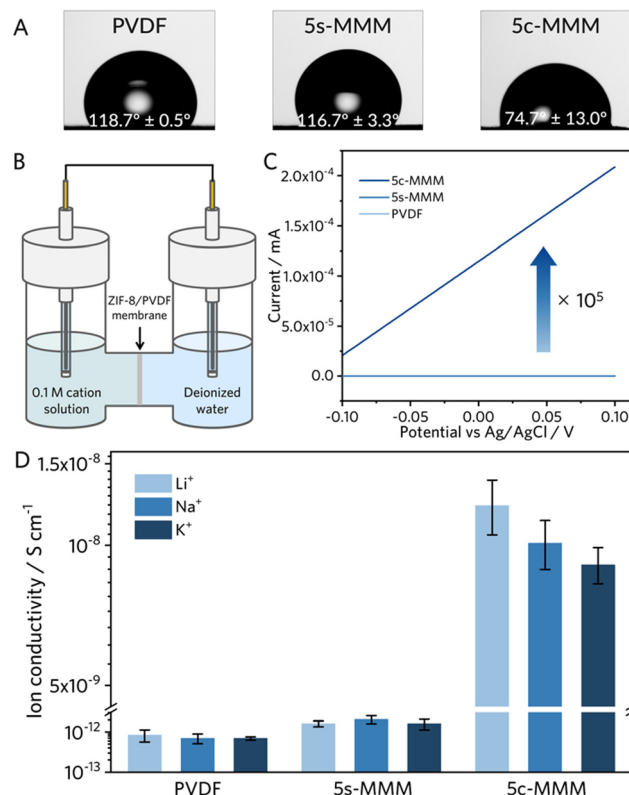

Fig. 4 (A) Water contact angle measurements of PVDF, 5s-MMM and 5c-MMM surfaces. (B) Schematic of H-cell for measuring ion conductivity. (C) The current–voltage curve of PVDF, 5s-MMM, and 5c-MMM measured in an H-cell with 0.1 M Li ion concentration gradient across the MMM. (D) Ion conductivity extrapolated from LSV measurements and normalized to aqueous ion mobility.

ion conductivities of LiCl, NaCl, and KCl electrolytes in the absence of MMMs for calibration (Fig. S6, see ESI† for details).

LSV measurements of both PVDF and 5s-MMMs recorded minimal current response, with Li ion conductivities on the order of 10^{-13} S cm^{-1} and 10^{-12} S cm^{-1} respectively, retaining negligible transport selectivity (Fig. 4C and Fig. S7, S8, ESI†). The 5c-MMM, however, exhibited a significant enhancement to the measured ionic conductivity, improving nearly four orders of magnitude from the 5s-MMM ($\sim 10^{-8}$ S cm^{-1}) (Fig. 4D and Fig. S9, S10, ESI†). This enhancement further supports our hypothesis, where the observed crystalline evolution increases the surface hydrophilicity to favour ion conduction. In addition to the improved conductivity, a selective transport sequence of alkali ion transport, Li$^+$ > Na$^+$ > K$^+$ indeed arose in the 5c-MMM (Fig. 4D). These results indicate enhanced mass transport control at ZIF-8 crystal facets, potentially due to the subnanoporous sieving effect. This effect is promoted by densely continuous ion transport pathways formed through the ZIF-8's interpenetrated morphology, leading to preferential partial dehydration of larger Li ions compared to other alkali ions. (Fig. 1B). To further probe the significance of ZIF-8's interpenetrated microstructures on selective Li ion transport, we prepared 5c-MMM samples with a crystallization truncated from 16 hours to 4 hours. The resulting MMMs, further denoted

This journal is © The Royal Society of Chemistry 2024

J. Mater. Chem. C, 2024, **12**, 13816–13821 | **13819**

as 5c-MMM-4h, exhibited discontinuous crystal growth of much smaller crystallites ($\sim$1–5 μm), with only few larger crystallites produced on the surface of the sample (Fig. S12A, ESI†). Contact angles were recorded highlighting the lack of surface hydrophilicity with a truncated reaction time (Fig. S12B, ESI†). Similar to the 5c-MMM with a full-scale crystallization, the 5c-MMM-4h exhibits an increase in ion conductivity, however, only 2-fold from the 5s-MMM nanocomposite (Fig. S10 and S12C, ESI†). The presence of the ZIF-8 helps to passivate hydrophobic PVDF domains thereby bolstering the ion conductivity, the 5c-MMM-4h is indiscriminate towards Li, Na, and K ions. Despite the improvement in ion mobility, the negligible transport selectivity towards the Li ion implies the necessitation of well-intergrown microstructures of the ZIF-8 to enable enthalpic discrimination of Na and K ions over Li ions, as a competitive mode of mass transport *via* ion partial dehydration.

Furthermore, we monitored time-dependent open circuit voltage (OCV) decay measurements of the 5c-MMM. Equilibration of the concentration gradient *via* ion diffusion through the MMM destroyed the H-cell's open circuit potential (E_{OC}), which was monitored over 12 hours by OCV measurement. 5c-MMM exhibited a sharper open circuit voltage decay in 0.1 M LiCl over 12 hours compared to NaCl and KCl electrolytes of equivalent concentration (Fig. S11, ESI†), further corroborating the unary Li ion-selective transport observed from LSV measurements. Finally, to confirm the feasibility of ZIF-8 based MMMs in aqueous environment, we performed stability tests by submerging the 5c-MMM in MilliQ water for 1 week. Powder x-ray diffraction patterns confirm the presence of the ZIF-8 with unperturbed crystallinity from its initial state (Fig. S13, ESI†).

Conclusions

This work demonstrates the seeded growth of interpenetrated ZIF-8 on a PVDF membrane for mass transport control of alkali ions. Leveraging the ZIF-8 as an effective nanoscopic seed yielded a simple process to effectively control the growth of microstructure and generate uniform nanocomposite membranes. The crystallization of the 5s-MMM transformed the composite properties from PVDF-dominant to ZIF-8-dominant, resulting in a greater hydrophilicity for aqueous transport and a 4-order enhancement to the Li ion conductivity from 5s-MMM. In addition, a dense interpenetrated morphology of the ZIF-8 facilitated ion transport through the apertures of the MOF network, exhibiting Li$^+$ selective transport over Na$^+$ and K$^+$, not present in the 5s-MMM or PVDF membrane. We expect to open new possibilities to fabricate diverse compositions and microstructures of MOF-incorporated composites for advanced membrane applications, including water purification, battery applications, and flexible electronics.

Author contributions

B. C. and J. P. designed and organized the project. B. C. conducted most characterizations. J. Y. C. performed XRD and SEM. C. W. and W. W. contributed to the synthesis of ZIF-8. B. C., J. Y. C., and J. P. wrote the manuscript. All authors contributed to writing the manuscript.

Data availability

The data supporting this article have been included as part of the ESI.†

Conflicts of interest

There are no conflicts to declare.

Acknowledgements

References

1 P. Greim, A. A. Solomon and C. Breyer, *Nat. Commun.*, 2020, **11**, 4570.

2 C. B. Tabelin, J. Dallas, S. Casanova, T. Pelech, G. Bournival, S. Saydam and I. Canbulat, *Miner. Eng.*, 2021, **163**, 106743.

3 K.-D. Kreuer and A. Münchinger, *Annu. Rev. Mater. Res.*, 2021, **51**, 21–46.

4 R. M. DuChanois, C. J. Porter, C. Violet, R. Verduzco and M. Elimelech, *Adv. Mater.*, 2021, **33**, 2101312.

5 A. Razmjou, M. Asadnia, E. Hosseini, A. Habibnejad Korayem and V. Chen, *Nat. Commun.*, 2019, **10**, 5793.

6 M. L. Vera, W. R. Torres, C. I. Galli, A. Chagnes and V. Flexer, *Nat. Rev. Earth Environ.*, 2023, **4**, 149–165.

7 A. Phan, C. J. Doonan, F. J. Uribe-Romo, C. B. Knobler, M. O'Keeffe and O. M. Yaghi, *Acc. Chem. Res.*, 2010, **43**, 58–67.

8 O. Yahgi, M. Kalmutzi and C. Diercks, *Introduction to Reticular Chemistry*, John Wiley & Sons, Ltd, 2019, pp. 463–479.

9 K. S. Park, Z. Ni, A. P. Côté, J. Y. Choi, R. Huang, F. J. Uribe-Romo, H. K. Chae, M. O'Keeffe and O. M. Yaghi, *PNAS*, 2006, **103**, 10186–10191.

10 G. Eisenman, J. Sandblom and E. Neher, *Biophys. J.*, 1978, **22**, 307–340.

11 H. Zhang, J. Hou, Y. Hu, P. Wang, R. Ou, L. Jiang, J. Z. Liu, B. D. Freeman, A. J. Hill and H. Wang, *Sci. Adv.*, 2018, **4**, eaaq0066.

12 J. Lu, X. Hu, K. M. Ung, Y. Zhu, X. Zhang and H. Wang, *Acc. Mater. Res.*, 2022, **3**, 735–747.

13 C. Zhang, Y. Mu, W. Zhang, S. Zhao and Y. Wang, *J. Membr. Sci.*, 2020, **596**, 117724.

14 Y. Zhang, X. Feng, S. Yuan, J. Zhou and B. Wang, *Inorg. Chem. Front.*, 2016, **3**, 896–909.

15 H. Yoo and N. Shin, *Appl. Surf. Sci.*, 2023, **625**, 157211.

16 H. T. Kwon and H.-K. Jeong, *J. Am. Chem. Soc.*, 2013, **135**, 10763–10768.

13820 | *J. Mater. Chem. C*, 2024, **12**, 13816–13821

This journal is © The Royal Society of Chemistry 2024

17 X. Wang, C. Chi, J. Tao, Y. Peng, S. Ying, Y. Qian, J. Dong, Z. Hu, Y. Gu and D. Zhao, *Chem. Commun.*, 2016, **52**, 8087–8090.

18 Y. Zhao, Y. Wei, L. Lyu, Q. Hou, J. Caro and H. Wang, *J. Am. Chem. Soc.*, 2020, **142**, 20915–20919.

19 J. Zhao, R. Fan, S. Xiang, J. Hu and X. Zheng, *Membranes*, 2023, **13**, 500.

20 L.-H. Xu, S.-H. Li, H. Mao, Y. Li, A.-S. Zhang, S. Wang, W.-M. Liu, J. Lv, T. Wang, W.-W. Cai, L. Sang, W.-W. Xie, C. Pei, Z.-Z. Li, Y.-N. Feng and Z.-P. Zhao, *Science*, 2022, **378**, 308–313.

21 M. Shah, H. T. Kwon, V. Tran, S. Sachdeva and H.-K. Jeong, *Microporous Mesoporous Mater.*, 2013, **165**, 63–69.

22 M. S. Attia, A. O. Youssef, M. N. Abou-Omar, E. H. Mohamed, R. Boukherroub, A. Khan, T. Altalhi and M. A. Amin, *Chemosphere*, 2022, **292**, 133369.

23 J. E. Marshall, A. Zhenova, S. Roberts, T. Petchey, P. Zhu, C. E. J. Dancer, C. R. McElroy, E. Kendrick and V. Goodship, *Polymers*, 2021, **13**, 1354.

24 A. Karimi, A. Khataee, V. Vatanpour and M. Safarpour, *Sep. Purif. Technol.*, 2020, **253**, 117548.

25 Y. Zhang, Y. Jia, M. Li and L. Hou, *Sci. Rep.*, 2018, **8**, 9597.

26 M. S. Denny, M. Kalaj, K. C. Bentz and S. M. Cohen, *Chem. Sci.*, 2018, **9**, 8842–8849.

27 J. T. Jung, J. F. Kim, H. H. Wang, E. di Nicolo, E. Drioli and Y. M. Lee, *J. Membr. Sci.*, 2016, **514**, 250–263.

28 X. Cai, T. Lei, D. Sun and L. Lin, *RSC Adv.*, 2017, **7**, 15382–15389.

29 A. C. Lopes, C. Ribeiro, V. Sencadas, G. Botelho and S. Lanceros-Méndez, *J. Mater. Sci.*, 2014, **49**, 3361–3370.

This journal is © The Royal Society of Chemistry 2024

J. Mater. Chem. C, 2024, **12**, 13816–13821 | **13821**